

# AGE-Net: Spectral–Spatial Fusion and Anatomical Graph Reasoning with Evidential Ordinal Regression for Knee Osteoarthritis Grading

Xiaoyang Li\* Runni Zhou\*

College of Medicine and Biological Information Engineering, Northeastern University, Shenyang 110016, China.

## Abstract

Automated Kellgren–Lawrence (KL) grading from knee radiographs is challenging due to subtle structural changes, long-range anatomical dependencies, and ambiguity near grade boundaries. We propose AGE-Net, a ConvNeXt-based framework integrating Spectral–Spatial Fusion (SSF), Anatomical Graph Reasoning (AGR), and Differential Refinement (DFR). To capture predictive uncertainty and preserve label ordinality, AGE-Net further employs a Normal–Inverse-Gamma (NIG) evidential regression head (COE-Head) and a pairwise ordinal ranking constraint. On a knee KL dataset, AGE-Net achieves QWK  $0.9017 \pm 0.0045$  and MSE  $0.2349 \pm 0.0028$  (3 seeds), improving over strong CNN baselines and confirming consistent gains in ablation studies. We additionally outline uncertainty quality, robustness, and explainability analyses and reserve space for upcoming experimental figures.

**Keywords:** Knee osteoarthritis; Kellgren–Lawrence grading; Ordinal regression; Graph reasoning; Evidential learning; Uncertainty

---

\*These authors contributed equally to this work.

# 1 Introduction

Knee osteoarthritis (OA) is among the most prevalent degenerative musculoskeletal disorders, imposing substantial burden through chronic pain, reduced mobility, and diminished quality of life. Radiographic Kellgren–Lawrence (KL) grading [Kellgren and Lawrence \[1957\]](#) remains one of the most widely adopted clinical standards to characterize OA severity, typically ranging from Grade 0 (no OA) to Grade 4 (severe OA). Automating KL grading from plain radiographs could reduce workload and inter-observer variation and facilitate population-scale screening.

Despite progress in deep learning for radiography, reliable KL grading remains difficult due to three recurring challenges. First, KL transitions may be driven by subtle and localized findings, such as early osteophytes or mild joint space narrowing, frequently embedded in low-contrast anatomical contexts. Second, OA severity is influenced by long-range anatomical structure: medial and lateral compartments, tibiofemoral alignment, and spatially distributed textural cues jointly contribute to an overall grade, which can be under-modeled by strictly local operations. Third, KL labels are ordinal and inherently uncertain near boundaries; borderline cases are common, and label noise is non-negligible even among expert readers. A clinically useful system should thus (i) preserve monotonic ordering across grades and (ii) represent uncertainty that correlates with ambiguity and error.

Modern CNN backbones (e.g., ConvNeXt [Liu et al. \[2022\]](#)) provide strong feature extraction, but end-to-end pipelines often treat KL as plain classification and do not explicitly model anatomy-aligned long-range dependencies, nor do they provide calibrated uncertainty. We propose **AGE-Net**, a ConvNeXt-based framework with four key components: (1) **Spectral–Spatial Fusion (SSF)** for frequency-sensitive and spatially recalibrated enhancement; (2) **Anatomical Graph Reasoner (AGR)** to model long-range anatomical relations by graph message passing on pooled tokens; (3) **Differential Refiner (DFR)** to emphasize edge- and boundary-sensitive cues that often indicate joint degeneration; and (4) **COE-Head** evidential NIG regression [Amini et al. \[2020\]](#) plus a **pairwise ordinal ranking constraint** to enforce ordinal consistency and support uncertainty-aware decision making.

(a) Spectral-Spatial Fusion and Anatomical Graph Reasoning for Ordinal Knee Osteoarthritis Grading

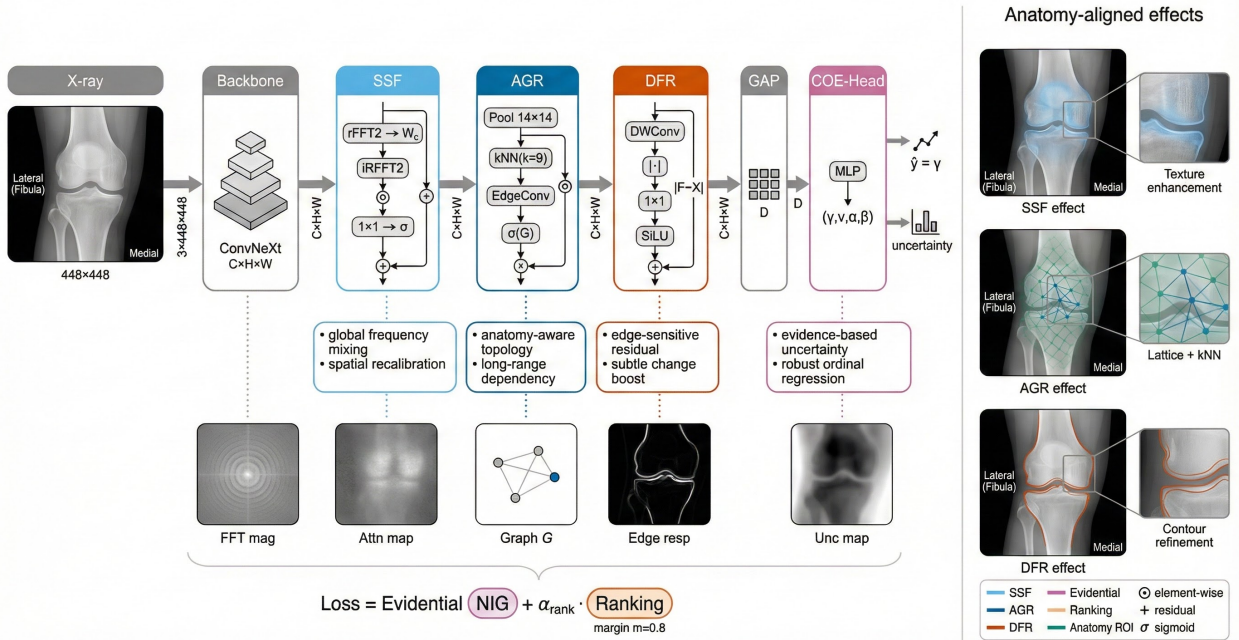


**Figure 1:** AGE-Net overview. A ConvNeXt backbone extracts feature maps, followed by SSF, AGR, and DFR. Global average pooling yields an embedding fed to the COE evidential head to produce NIG parameters. Training optimizes evidential loss plus ordinal ranking.

**Contributions.** This paper makes the following contributions:

- We introduce AGE-Net, a unified KL grading framework integrating SSF, AGR, and DFR on top of a strong ConvNeXt backbone [Liu et al. \[2022\]](#).
- We incorporate evidential NIG regression [Amini et al. \[2020\]](#) and a pairwise ordinal ranking constraint to improve uncertainty modeling and ordinal consistency.
- We report strong empirical performance with ablation evidence and reserve additional experiments (uncertainty quality, robustness, explainability) with dedicated figure placeholders for ongoing work.

## 2 Related Work

### 2.1 Backbones for radiographs and medical imaging

CNN backbones such as VGG [Simonyan and Zisserman \[2015\]](#), ResNet [He et al. \[2016\]](#), DenseNet [Huang et al. \[2017\]](#), and Inception [Szegedy et al. \[2016\]](#) are common choices in radiograph analysis. EfficientNet [Tan and Le \[2019\]](#) improves scaling and parameter efficiency. ConvNeXt [Liu et al. \[2022\]](#) modernizes ConvNet design and offers strong transfer learning performance. Vision Transformers such as ViT [Dosovitskiy et al. \[2021\]](#) and Swin [Liu et al. \[2021\]](#) provide global modeling, but can be sensitive to pretraining and optimization, especially in medical domains with limited labeled data and distribution shifts.

### 2.2 Ordinal regression and ranking constraints

KL grades are ordinal; treating them as independent classes can yield inconsistent decision boundaries and suboptimal calibration around adjacent grades. Ordinal learning frameworks, including rank-consistent formulations like CORAL [Cao et al. \[2020\]](#), aim to preserve monotonic structure. Pairwise ranking constraints provide a practical mechanism to enforce ordering by penalizing violations on valid grade-separated pairs.

### 2.3 Graph reasoning for non-local dependencies

Graph neural networks (GNNs) and related message passing mechanisms can explicitly model non-local dependencies among tokens or anatomical regions. EdgeConv and dynamic graph construction ideas (e.g., DGCNN) [Wang et al. \[2019\]](#) motivate our anatomy-aware graph reasoning over pooled radiographic tokens.

## 2.4 Uncertainty estimation and evidential learning

Uncertainty estimation is critical for borderline and ambiguous KL cases. Evidential learning [Amini et al. \[2020\]](#) enables deterministic prediction of distributional parameters without sampling-heavy Bayesian inference, making it attractive for practical deployment and uncertainty-aware triage.

# 3 Method

## 3.1 Problem formulation

We consider ordinal KL grading with labels  $y \in \{0, 1, 2, 3, 4\}$ . Instead of treating grades as independent classes, we produce a continuous score  $\gamma \in \mathbb{R}$  and map to grade by rounding/clipping during evaluation. The model should (i) predict accurate scores and (ii) reflect uncertainty associated with ambiguous cases.

## 3.2 Backbone and feature map

Given an input radiograph  $x \in \mathbb{R}^{3 \times H_0 \times W_0}$ , the ConvNeXt backbone [Liu et al. \[2022\]](#) outputs a deep feature map

$$F = f_{\text{bb}}(x) \in \mathbb{R}^{C \times H \times W}. \quad (1)$$

AGE-Net augments  $F$  with three enhancement modules (SSF, AGR, DFR), followed by global pooling and a prediction head.

## 3.3 Spectral–Spatial Fusion (SSF)

**Motivation.** Radiographic OA cues often manifest as texture variations and subtle contrast changes. Convolutional features can underutilize global frequency context. SSF introduces lightweight global frequency mixing and spatial recalibration, encouraging the model to capture both textural patterns (frequency domain) and anatomy-aligned emphasis (spatial domain).

**Spectral path.** Let  $\mathcal{F}(\cdot)$  denote the 2D Fourier transform (implemented via rFFT for real signals). We compute

$$\hat{F} = \mathcal{F}(F). \quad (2)$$

We apply channel-wise learnable complex scaling  $W_c \in \mathbb{C}$ :

$$\hat{F}'_c = \hat{F}_c \odot W_c, \quad F_{\text{spec}} = \mathcal{F}^{-1}(\hat{F}'). \quad (3)$$

This performs a global, channel-wise frequency reweighting that can boost frequency components linked to fine-grained radiographic texture.

**Spatial attention path.** We compute a spatial gate  $A = \sigma(g(F))$ , where  $g$  is a lightweight  $1 \times 1$  bottleneck:

$$A = \sigma(\text{Conv}_{1 \times 1}(\phi(\text{BN}(\text{Conv}_{1 \times 1}(F))))), \quad (4)$$

with  $\phi(\cdot)$  a nonlinearity (e.g., ReLU), and  $\sigma(\cdot)$  sigmoid.

**Fusion.** The fused output uses a residual stabilization:

$$\text{SSF}(F) = F + F_{\text{spec}} + (F \odot A). \quad (5)$$

Residual addition mitigates optimization instability and preserves backbone semantics, while enabling SSF to act as a learnable enhancement.

**Complexity.** SSF adds negligible parameters (complex scale per channel plus two  $1 \times 1$  conv layers). FFT cost is  $O(CHW \log(HW))$  but remains practical at the feature-map resolution (post-backbone) and is amortized across training.

### 3.4 Anatomical Graph Reasoner (AGR)

**Motivation.** KL grading depends on relationships across anatomical compartments. Standard convolutions may fail to integrate long-range structure efficiently. AGR constructs an anatomy-aware token graph from pooled features and performs message passing to capture non-local dependencies.

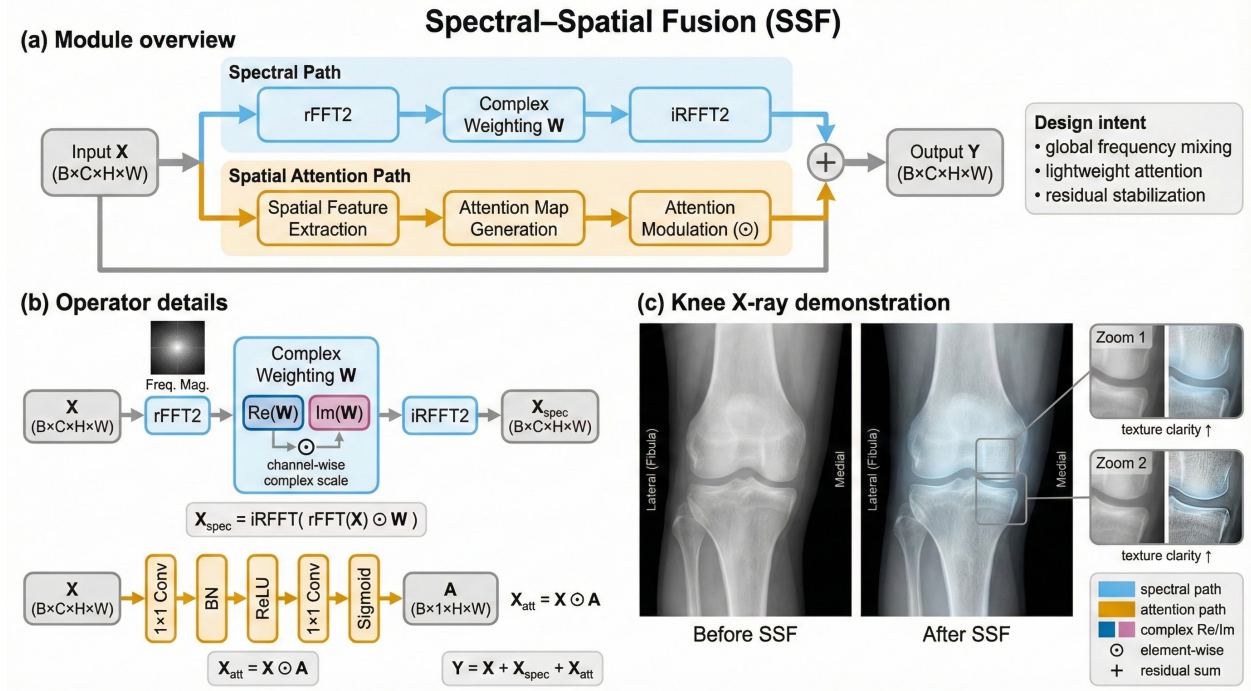


**Figure 2:** Spectral–Spatial Fusion (SSF). SSF performs frequency-domain modulation (rFFT/iFFT with learnable complex weights) and spatial attention recalibration with residual stabilization.

**Tokenization.** We reduce channels and pool to a fixed grid:

$$F_r = \text{Conv}_{1 \times 1}(F) \in \mathbb{R}^{C_r \times H \times W}, \quad F_p = \text{Pool}_{14 \times 14}(F_r) \in \mathbb{R}^{C_r \times 14 \times 14}. \quad (6)$$

Flatten spatially to obtain  $N = 196$  node features:

$$X \in \mathbb{R}^{C_r \times N}, \quad N = 14 \times 14. \quad (7)$$

**kNN graph construction.** We build a kNN graph in feature space (k=9). For each node  $i$ , neighbors  $\mathcal{N}(i)$  are selected by nearest distances, creating an adaptive topology that can align with anatomical variability.

**EdgeConv-style aggregation.** Inspired by DGCNN [Wang et al. \[2019\]](#), we compute edge features

$$e_{ij} = h_\theta([x_i, x_j - x_i]), \quad j \in \mathcal{N}(i), \quad (8)$$

where  $h_\theta$  is a shared MLP (implemented as  $1 \times 1$  conv + BN + LeakyReLU). Aggregation uses

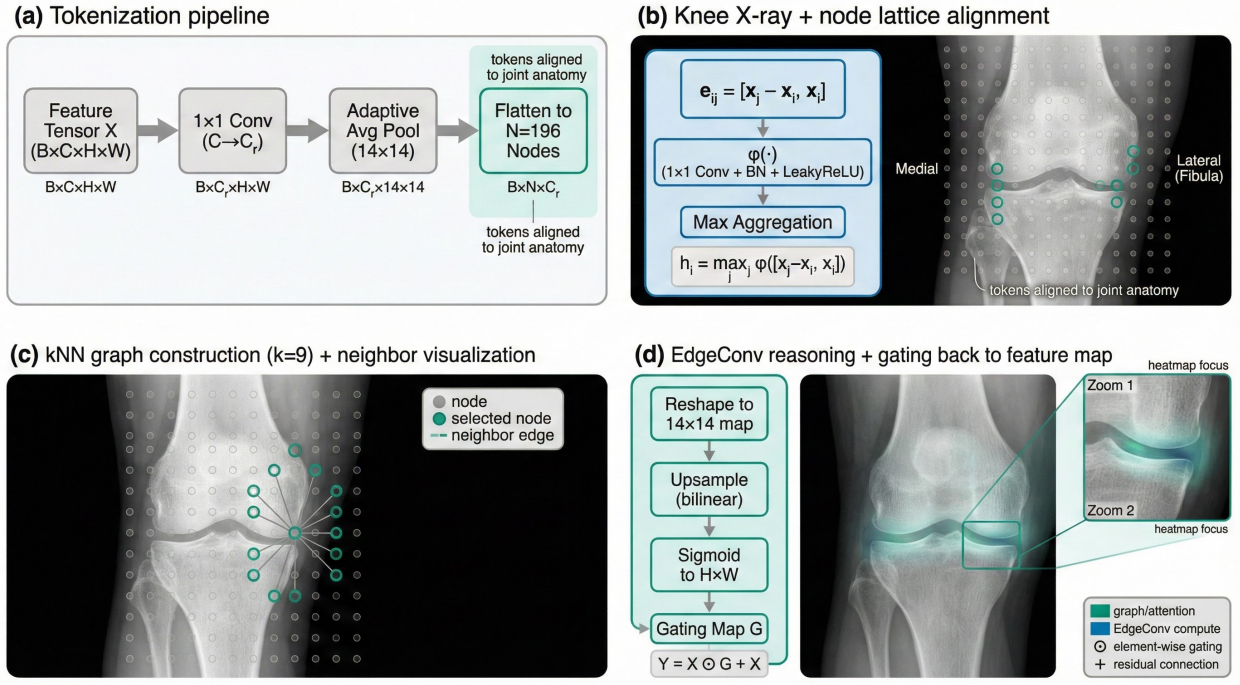


**Figure 3:** Anatomical Graph Reasoner (AGR). Features are pooled to a fixed grid, flattened into tokens, and processed via kNN graph + EdgeConv-style aggregation. A sigmoid gate is upsampled and applied to the original feature map with residual connection.

max pooling:

$$x'_i = \max_{j \in \mathcal{N}(i)} e_{ij}. \quad (9)$$

We reshape  $\{x'_i\}$  back to  $14 \times 14$  and upsample to  $(H, W)$ , then map to a gate  $G$ :

$$G = \sigma(\text{BN}(\text{Conv}_{1 \times 1}(\text{Upsample}(X')))) \in \mathbb{R}^{C \times H \times W}. \quad (10)$$

**Gated residual.** AGR returns

$$\text{AGR}(F) = F \odot G + F. \quad (11)$$

The gate emphasizes anatomy-aligned features while preserving base representation.

**Complexity.** Graph building costs  $O(BN^2)$  for naive pairwise distances; with  $N = 196$  this is manageable. Message passing scales with  $O(BNkC_r)$  and is lightweight compared with backbone compute.

### 3.5 Differential Refiner (DFR)

**Motivation.** OA severity is often indicated by boundary and edge changes (e.g., joint space narrowing contours). DFR explicitly highlights differential responses between a depthwise-filtered feature and the original feature map, encouraging sensitivity to subtle structural transitions.

**Depthwise response and differential.** We compute a depthwise response  $F_d$ :

$$F_d = \text{DWConv}_{3 \times 3}(F), \quad (12)$$

and define an edge-like differential map

$$E = |F_d - F|. \quad (13)$$

**Channel mixing and stabilization.** We apply a  $1 \times 1$  mixing conv and normalization:

$$R = \text{BN}(\text{Conv}_{1 \times 1}(E)). \quad (14)$$

Finally, DFR outputs a residual nonlinearity:

$$\text{DFR}(F) = \text{SiLU}(R + F). \quad (15)$$

**Interpretation.** The absolute difference acts like a learned gradient operator in feature space, while the residual ensures that DFR acts as refinement rather than a destructive transform.

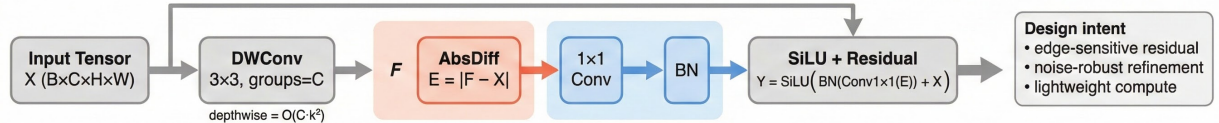
**Complexity.** DFR adds one depthwise conv and one pointwise conv per block; parameter overhead is modest and suitable for high-resolution inputs.

### 3.6 COE-Head: Evidential NIG Regression

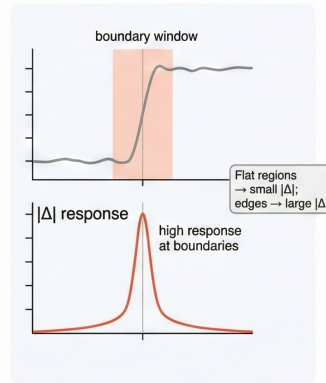
**Motivation.** Borderline KL cases are intrinsically ambiguous; a model should not only output a score, but also express uncertainty. Evidential regression [Amini et al. \[2020\]](#) predicts distributional

## Differential Feature Refinement (DFR) Module

### (a) Operator Pipeline



### (b) Mechanism Visualization



### (c) Knee X-ray Demonstration

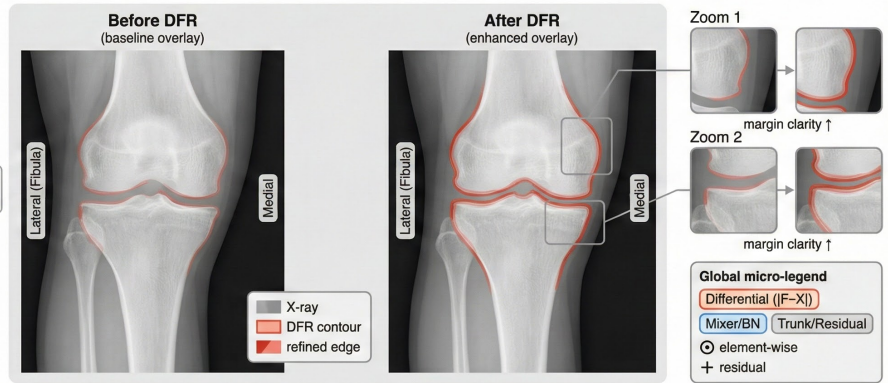


**Figure 4:** Differential Refiner (DFR). DFR uses depthwise filtering and absolute feature difference to enhance boundary-sensitive cues.

parameters that capture both aleatoric and epistemic uncertainty signals in a deterministic forward pass.

**Parameterization.** The COE head maps pooled embedding  $z \in \mathbb{R}^C$  to four parameters:

$$(\gamma, \nu, \alpha, \beta) = h_{\text{coe}}(z), \quad (16)$$

where  $\gamma$  is the predictive mean, and  $(\nu, \alpha, \beta)$  define the Normal-Inverse-Gamma prior. We enforce positivity constraints via softplus:

$$\nu = \text{softplus}(\cdot) + \epsilon, \quad \alpha = \text{softplus}(\cdot) + 1 + \epsilon, \quad \beta = \text{softplus}(\cdot) + \epsilon. \quad (17)$$

**Predictive uncertainty.** Under NIG, the induced predictive distribution is a Student- $t$ ; a commonly used predictive variance is

$$\text{Var}(y) = \frac{\beta(1 + \nu)}{\nu(\alpha - 1)}, \quad \alpha > 1. \quad (18)$$

## COE-Head: Evidential NIG Regression

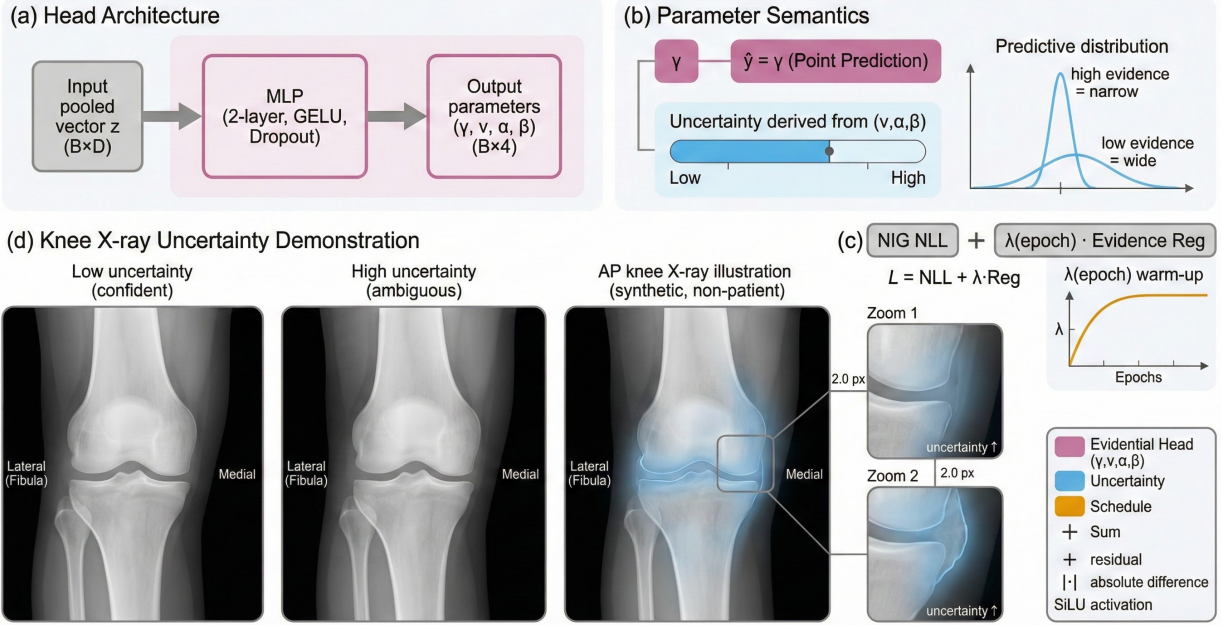


**Figure 5:** COE-Head: evidential NIG regression. The head predicts  $(\gamma, v, \alpha, \beta)$  and derives uncertainty from evidence parameters.

Higher evidence ( $v, \alpha$ ) typically yields narrower predictive distributions.

**Loss.** We optimize NIG negative log-likelihood plus evidence regularization:

$$\mathcal{L}_{\text{evi}} = \mathcal{L}_{\text{NLL}} + \lambda(t) |y - \gamma| (2v + \alpha), \quad (19)$$

with warm-up schedule  $\lambda(t) = 0.03 \cdot \min(1, \frac{t}{20})$  matching the current training code.

### 3.7 Ordinal Ranking Constraint

**Motivation.** KL grades encode monotonic severity; ordinal consistency is important to avoid implausible outputs (e.g., predicting lower score for obviously more severe images). Pairwise constraints provide a direct mechanism to enforce ordering.

**Valid pairs and margin.** For a mini-batch, define the set of valid pairs

$$\Omega = \{(i, j) \mid y_i - y_j \geq 1\}. \quad (20)$$

## Ordinal Ranking Constraint

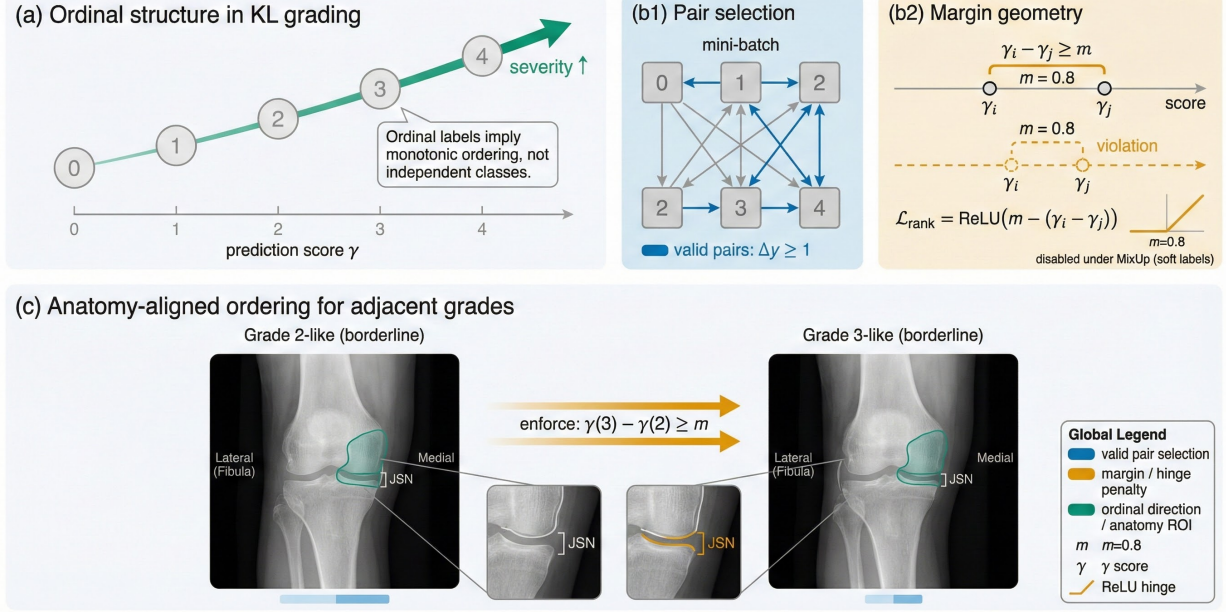


**Figure 6:** Ordinal ranking constraint. The ranking loss enforces a margin on valid grade-separated pairs to preserve monotonic ordering.

We enforce a margin  $m = 0.8$  on scores:

$$\mathcal{L}_{\text{rank}} = \frac{1}{|\Omega|} \sum_{(i,j) \in \Omega} \max(0, m - (\gamma_i - \gamma_j)). \quad (21)$$

We disable ranking under Mixup because labels become soft and the pairwise inequality becomes ill-defined, consistent with the current implementation.

**Total objective.** The final training objective is

$$\mathcal{L} = \mathcal{L}_{\text{evi}} + \alpha_{\text{rank}} \mathcal{L}_{\text{rank}}, \quad (22)$$

with  $\alpha_{\text{rank}} = 2.0$  in our experiments.

### 3.8 End-to-end pipeline

Let  $F_0 = f_{\text{bb}}(x)$  and apply modules sequentially:

$$F_1 = \text{SSF}(F_0), \quad F_2 = \text{AGR}(F_1), \quad F_3 = \text{DFR}(F_2). \quad (23)$$

We pool  $F_3$  to embedding  $z$ , predict NIG parameters via COE, and compute total loss  $\mathcal{L}$ . In ablations, we disable each module by removing its transform from the sequence.

## 4 Experiments

### 4.1 Dataset and evaluation protocol

We evaluate on a knee radiograph dataset with KL labels  $\{0, 1, 2, 3, 4\}$ . We repeat all runs with 3 random seeds and report mean $\pm$ std. **(TBD)** We will document dataset size, acquisition protocol, per-grade distribution, and patient-level split strategy to avoid subject leakage across train/val/test sets.

### 4.2 Implementation details

Inputs are resized to  $512 \times 512$  and randomly cropped to  $448 \times 448$ . We train for 300 epochs using AdamW [Loshchilov and Hutter \[2019\]](#) with cosine annealing [Loshchilov and Hutter \[2017\]](#). We apply RandomAffine and ColorJitter augmentations, Mixup [Zhang et al. \[2018\]](#) with probability 0.5, and Random Erasing [Zhong et al. \[2020\]](#) with probability 0.25. Training uses mixed precision and EMA (decay 0.999). Test-time augmentation (TTA) averages predictions of an image and its horizontal flip.

**Table 1:** Training configuration (from the current implementation).

Item	Setting
Backbone	ConvNeXt-Base <a href="#">Liu et al. [2022]</a> (offline weights)
Input size	$448 \times 448$
Epochs	300
Optimizer	AdamW <a href="#">Loshchilov and Hutter [2019]</a>
Base LR	$1 \times 10^{-5}$ (head), backbone $0.2 \times$
Schedule	Cosine annealing <a href="#">Loshchilov and Hutter [2017]</a>
Weight decay	$1 \times 10^{-5}$
EMA	decay 0.999
Mixup	$p = 0.5$ <a href="#">Zhang et al. [2018]</a>
Random Erasing	$p = 0.25$ <a href="#">Zhong et al. [2020]</a>
TTA	flip average
Ranking	$\alpha_{\text{rank}} = 2.0, m = 0.8$

### 4.3 Metrics

We report quadratic weighted kappa (QWK) [Cohen \[1968\]](#), mean squared error (MSE), accuracy (ACC), macro-F1, and recall. For QWK/ACC/F1/Recall, continuous predictions are rounded to nearest integer grade and clipped to  $[0, 4]$ .

## 5 Results

### 5.1 Main comparison

Table 2 reports that AGE-Net achieves the best overall performance (QWK  $0.9017 \pm 0.0045$ ; MSE  $0.2349 \pm 0.0028$ ) compared with strong CNN baselines and representative transformer baselines under our current setting.

### 5.2 Ablation study

Table 3 isolates the effect of major components. Removing ranking decreases QWK, consistent with the importance of explicit ordinal constraints. Removing AGR leads to a larger drop, highlighting the value of anatomy-aware long-range reasoning.

**Table 2:** Main comparison (mean $\pm$ std over seeds).

Method	QWK $\uparrow$	MSE $\downarrow$	ACC $\uparrow$	F1 $\uparrow$	Rec $\uparrow$
<b>AGE-Net (Full)</b>	<b>0.9017<math>\pm</math>0.0045</b>	<b>0.2349<math>\pm</math>0.0028</b>	<b>0.7839<math>\pm</math>0.0056</b>	<b>0.8012<math>\pm</math>0.0053</b>	<b>0.7919<math>\pm</math>0.0060</b>
AGE-Net (w/o Rank)	0.8963 $\pm$ 0.0033	0.2600 $\pm$ 0.0083	0.7738 $\pm$ 0.0056	0.7893 $\pm$ 0.0067	0.7797 $\pm$ 0.0056
AGE-Net (w/o AGR)	0.8932 $\pm$ 0.0018	0.2665 $\pm$ 0.0017	0.7682 $\pm$ 0.0107	0.7786 $\pm$ 0.0131	0.7634 $\pm$ 0.0149
AGE-Net (Base ConvNeXt)	0.8909 $\pm$ 0.0113	0.2795 $\pm$ 0.0287	0.7701 $\pm$ 0.0051	0.7774 $\pm$ 0.0273	0.7632 $\pm$ 0.0373
VGG16 <a href="#">Simonyan and Zisserman [2015]</a>	0.8654 $\pm$ 0.0069	0.3046 $\pm$ 0.0102	0.7154 $\pm$ 0.0089	0.7180 $\pm$ 0.0170	0.6955 $\pm$ 0.0165
EfficientNet <a href="#">Tan and Le [2019]</a>	0.8638 $\pm$ 0.0012	0.3078 $\pm$ 0.0060	0.7087 $\pm$ 0.0049	0.7166 $\pm$ 0.0050	0.6939 $\pm$ 0.0058
ConvNeXt-Base <a href="#">Liu et al. [2022]</a>	0.8602 $\pm$ 0.0077	0.3248 $\pm$ 0.0118	0.7132 $\pm$ 0.0087	0.7295 $\pm$ 0.0019	0.7298 $\pm$ 0.0039
Inception-V3 <a href="#">Szegedy et al. [2016]</a>	0.8475 $\pm$ 0.0075	0.3252 $\pm$ 0.0069	0.6752 $\pm$ 0.0030	0.6855 $\pm$ 0.0093	0.6590 $\pm$ 0.0113
DenseNet121 <a href="#">Huang et al. [2017]</a>	0.8427 $\pm$ 0.0088	0.3274 $\pm$ 0.0032	0.6629 $\pm$ 0.0126	0.6010 $\pm$ 0.0191	0.5750 $\pm$ 0.0189
ResNet50 <a href="#">He et al. [2016]</a>	0.8271 $\pm$ 0.0012	0.3711 $\pm$ 0.0021	0.6272 $\pm$ 0.0033	0.5932 $\pm$ 0.0251	0.5629 $\pm$ 0.0195
Swin-T <a href="#">Liu et al. [2021]</a>	0.5603 $\pm$ 0.0329	0.7767 $\pm$ 0.0493	0.3531 $\pm$ 0.0140	0.2935 $\pm$ 0.0179	0.3363 $\pm$ 0.0101
ViT-B <a href="#">Dosovitskiy et al. [2021]</a>	0.3473 $\pm$ 0.0298	1.0413 $\pm$ 0.0084	0.2682 $\pm$ 0.0168	0.1612 $\pm$ 0.0217	0.2519 $\pm$ 0.0112

**Table 3:** Ablation (mean $\pm$ std over 3 seeds).

Variant	QWK $\uparrow$	MSE $\downarrow$
<b>Full</b>	<b>0.9017<math>\pm</math>0.0045</b>	<b>0.2349<math>\pm</math>0.0028</b>
w/o Rank	0.8963 $\pm$ 0.0033	0.2600 $\pm$ 0.0083
w/o AGR	0.8932 $\pm$ 0.0018	0.2665 $\pm$ 0.0017
Base ConvNeXt	0.8909 $\pm$ 0.0113	0.2795 $\pm$ 0.0287
<i>(TBD) w/o SSF</i>	–	–
<i>(TBD) w/o DFR</i>	–	–
<i>(TBD) w/o COE (heteroscedastic)</i>	–	–

### 5.3 Per-grade analysis (planned / in-progress)

We will add per-grade precision/recall and confusion matrices to better characterize borderline failure modes (e.g., confusion between grades 1/2/3). These analyses often reveal whether improvements concentrate on adjacent grade disambiguation.

### 5.4 Uncertainty quality (planned / in-progress)

To validate uncertainty, we will evaluate: (i) binned uncertainty vs. absolute error; (ii) selective prediction via risk–coverage curves; (iii) correlation metrics (Spearman/Pearson) between uncertainty and error.

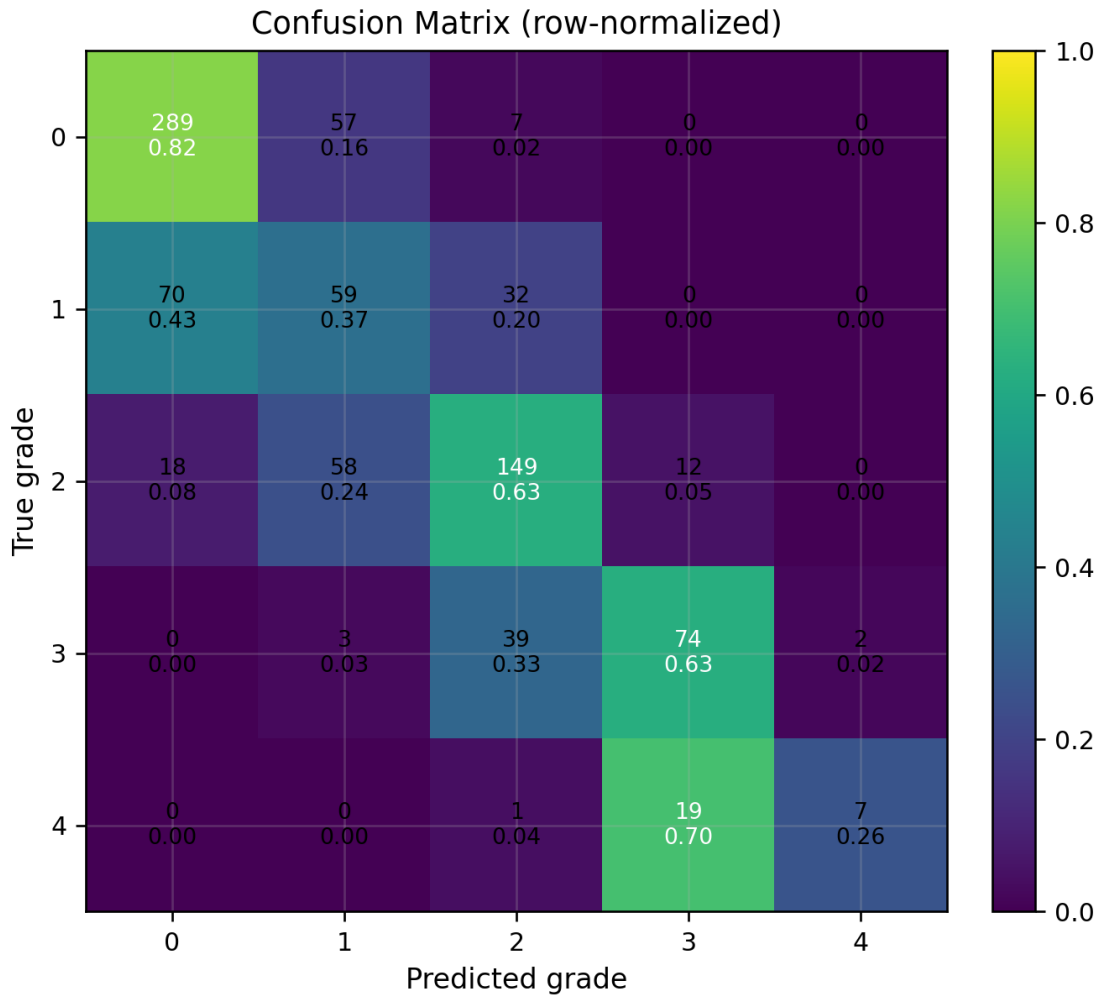


**Figure 7:** Per-grade analysis placeholder: confusion matrix and per-grade performance breakdown.

## 5.5 Robustness under perturbations (planned / in-progress)

We will evaluate robustness under brightness/contrast shifts, Gaussian noise, blur, and occlusion.

We will report QWK/MSE degradation curves and compare baseline vs. AGE-Net to quantify resilience benefits from SSF/DFR/AGR.

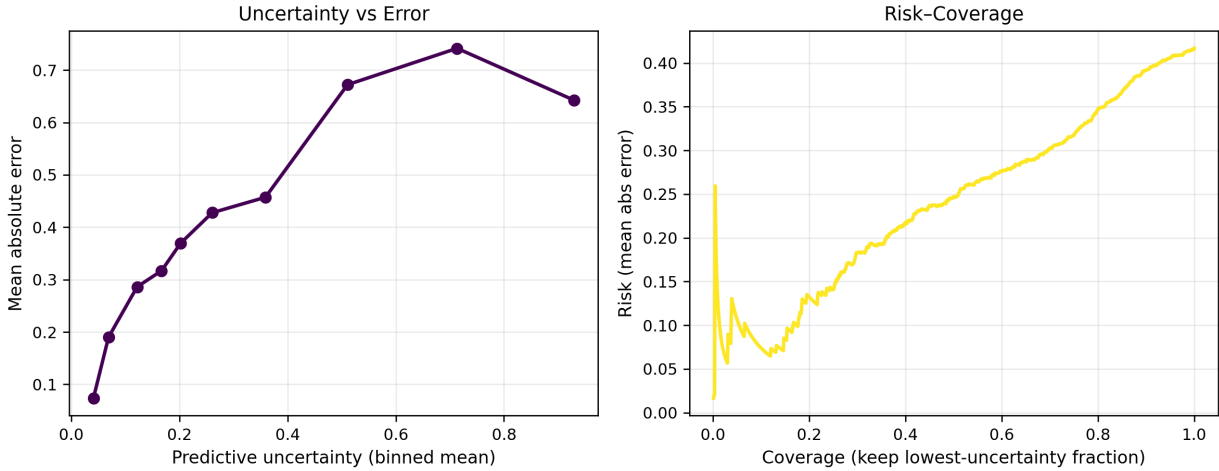


**Figure 8:** Uncertainty evaluation placeholder: calibration-like plot and risk–coverage curve.

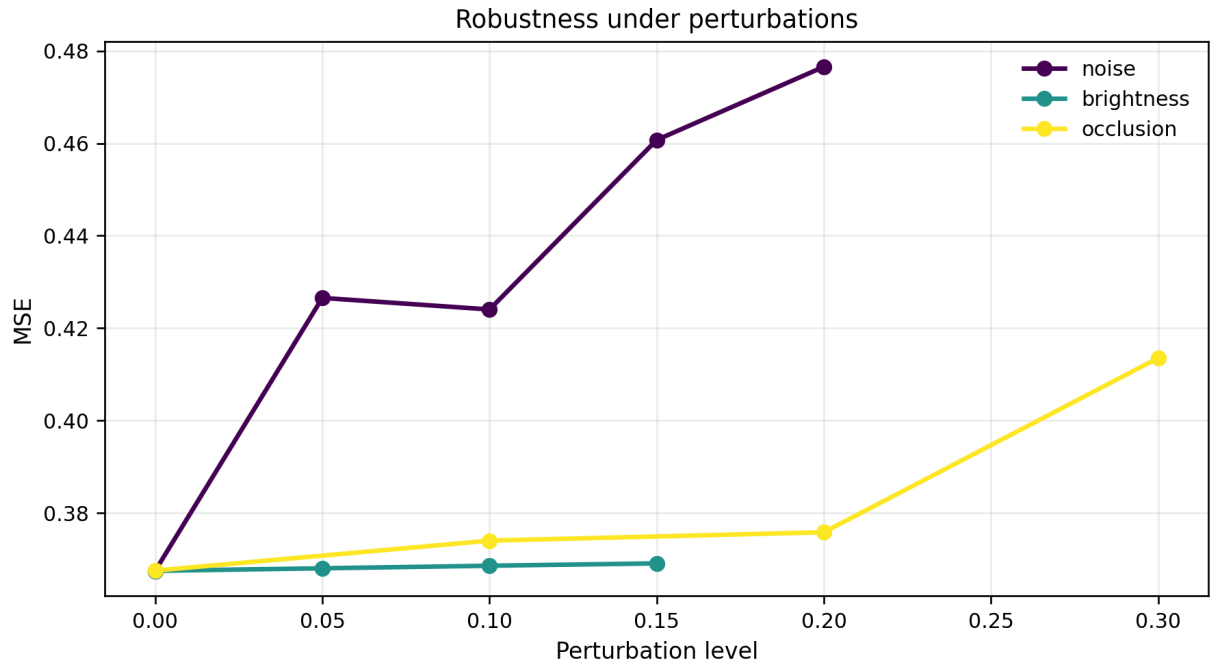


**Figure 9:** Robustness evaluation placeholder under perturbations.

## 6 Discussion

### 6.1 Why SSF helps

SSF provides global frequency mixing and spatial recalibration. In radiographs, fine texture patterns and subtle contrast differences can be critical for early OA cues. Frequency-domain modulation enables the model to learn global spectral emphasis, while spatial gating focuses enhancement on

informative regions. The residual design stabilizes optimization and keeps SSF lightweight.

## 6.2 Why AGR helps

AGR explicitly introduces non-local reasoning over pooled tokens. This is particularly relevant for tibiofemoral joint assessment, where cues span multiple compartments. By constructing kNN graphs in feature space, AGR can adapt its neighborhood structure to anatomical variability and encode long-range relations beyond fixed receptive fields. The gating mechanism provides an interpretable pathway for anatomy-aligned emphasis.

## 6.3 Why DFR helps

DFR targets edge- and boundary-sensitive cues. KL grading relies on joint space narrowing and contour changes; feature differentials can highlight precisely such transitions. Unlike heavy edge detectors in pixel space, DFR learns edge sensitivity in feature space and integrates seamlessly with residual learning.

## 6.4 Uncertainty and ordinality

COE evidential regression provides a mechanism to represent uncertainty that can be used for triage (e.g., defer high-uncertainty cases). The ranking constraint enforces monotonicity and combats degenerate regressors that might fit MSE while violating grade ordering. Together, they align the predictor with clinical expectations: ordinal consistency and uncertainty awareness.

## 6.5 Limitations and future work

First, we will complete uncertainty calibration, robustness testing, and explainability analyses and include the corresponding figures. Second, transformer baselines may require stronger pretraining or alternative optimization; we will add tuned versions and report results. Third, generalization

across acquisition sites and demographic subgroups will be studied with external validation if available.

## 7 Conclusion

We presented AGE-Net for ordinal KL grading from knee radiographs. AGE-Net integrates SSF, AGR, and DFR with a COE evidential NIG head and an ordinal ranking constraint. The method achieves strong performance (QWK  $0.9017 \pm 0.0045$ ; MSE  $0.2349 \pm 0.0028$ ) and shows consistent improvements in ablations. Ongoing experiments will further quantify uncertainty quality, robustness, and interpretability.

## A Additional implementation notes

### A.1 Training tricks and stability

We adopt mixed precision training to improve throughput, and EMA to stabilize evaluation. Layer-wise learning rate decouples backbone and head updates: the backbone uses a smaller learning rate to reduce catastrophic forgetting of pretrained features, while the head learns task-specific mapping. We disable ranking loss under Mixup because labels become interpolated and the ordering constraint becomes ill-defined in soft label space.

### A.2 Test-time augmentation

We apply flip-based TTA by averaging predictions of the original and horizontally flipped inputs. This can reduce variance and improve robustness, especially for noisy radiographs.

## B Planned extended ablations

- **w/o SSF:** remove frequency modulation and spatial gating to isolate spectral contribution.

- **w/o DFR:** remove differential refinement to isolate boundary-sensitive enhancement.
- **w/o COE:** replace evidential head with heteroscedastic regression head and compare uncertainty quality.
- **k sensitivity:** vary k in AGR (e.g., 5/9/13) to study neighborhood size effects.
- **Token grid size:** vary pooling grid (e.g., 10×10, 14×14, 16×16).

## C Statistical significance (planned)

We will report paired significance tests across seeds (e.g., paired  $t$ -tests on per-seed QWK) and effect sizes when comparing full AGE-Net with major ablations and the ConvNeXt baseline.

## References

Alexander Amini, Wilko Schwarting, Ava Soleimany, and Daniela Rus. Deep evidential regression. In *Advances in Neural Information Processing Systems (NeurIPS)*, 2020.

Wei Cao, Vahid Mirjalili, and Sebastian Raschka. Rank consistent ordinal regression for neural networks with application to age estimation. *International Journal of Computer Vision*, 128: 3001–3014, 2020.

Jacob Cohen. Weighted kappa: Nominal scale agreement with provision for scaled disagreement or partial credit. *Psychological Bulletin*, 70(4):213–220, 1968.

Alexey Dosovitskiy, Lucas Beyer, Alexander Kolesnikov, Dirk Weissenborn, Xiaohua Zhai, Thomas Unterthiner, Mostafa Dehghani, Matthias Minderer, Georg Heigold, Sylvain Gelly, Jakob Uszkoreit, and Neil Houlsby. An image is worth 16x16 words: Transformers for image recognition at scale. In *International Conference on Learning Representations (ICLR)*, 2021.

Kaiming He, Xiangyu Zhang, Shaoqing Ren, and Jian Sun. Deep residual learning for image recognition. In *Proceedings of the IEEE Conference on Computer Vision and Pattern Recognition (CVPR)*, pages 770–778, 2016.

Gao Huang, Zhuang Liu, Laurens Van Der Maaten, and Kilian Q. Weinberger. Densely connected convolutional networks. In *Proceedings of the IEEE Conference on Computer Vision and Pattern Recognition (CVPR)*, 2017.

J. H. Kellgren and J. S. Lawrence. Radiological assessment of osteo-arthrosis. *Annals of the Rheumatic Diseases*, 16(4):494–502, 1957.

Ze Liu, Yutong Lin, Yue Cao, Han Hu, Yixuan Wei, Zheng Zhang, Stephen Lin, and Baining Guo. Swin transformer: Hierarchical vision transformer using shifted windows. In *Proceedings of the IEEE/CVF International Conference on Computer Vision (ICCV)*, pages 10012–10022, 2021.

Zhuang Liu, Hanzi Mao, Chao-Yuan Wu, Christoph Feichtenhofer, Trevor Darrell, and Saining Xie. A convnet for the 2020s. In *Proceedings of the IEEE/CVF Conference on Computer Vision and Pattern Recognition (CVPR)*, 2022.

Ilya Loshchilov and Frank Hutter. Sgdr: Stochastic gradient descent with warm restarts. In *International Conference on Learning Representations (ICLR)*, 2017.

Ilya Loshchilov and Frank Hutter. Decoupled weight decay regularization. In *International Conference on Learning Representations (ICLR)*, 2019.

Karen Simonyan and Andrew Zisserman. Very deep convolutional networks for large-scale image recognition. *International Conference on Learning Representations (ICLR)*, 2015.

Christian Szegedy, Vincent Vanhoucke, Sergey Ioffe, Jon Shlens, and Zbigniew Wojna. Rethinking the inception architecture for computer vision. In *Proceedings of the IEEE Conference on Computer Vision and Pattern Recognition (CVPR)*, pages 2818–2826, 2016.

Mingxing Tan and Quoc V. Le. Efficientnet: Rethinking model scaling for convolutional neural networks. In *International Conference on Machine Learning (ICML)*, 2019.

Yue Wang, Yongbin Sun, Ziwei Liu, Sanjay E. Sarma, Michael M. Bronstein, and Justin M. Solomon. Dynamic graph cnn for learning on point clouds. *ACM Transactions on Graphics*, 38(5), 2019.

Hongyi Zhang, Moustapha Cisse, Yann N. Dauphin, and David Lopez-Paz. mixup: Beyond empirical risk minimization. In *International Conference on Learning Representations (ICLR)*, 2018.

Zhun Zhong, Liang Zheng, Guoliang Kang, Shaozi Li, and Yi Yang. Random erasing data augmentation. In *AAAI Conference on Artificial Intelligence (AAAI)*, 2020.